Sound absorption enhancement in poro-elastic materials in the viscous regime using a mass–spring effect

Sound absorption enhancement in poro-elastic materials in the viscous regime using a mass-spring effect

S. Ahsani[a,b,c], C. Claeys[a,b], T. G. Zieliński[e], Ł. Jankowski[e], F. Scarpa[c,f], W. Desmet[a,b], E. Deckers[b,d]

[a] KU Leuven, Department of Mechanical Engineering, Division LMSD, Celestijnenlaan 300 - box 2420, Heverlee, Belgium
[b] DMMS Lab, Flanders Make, Heverlee, Belgium
[c] Bristol Composites Institute (ACCIS), University of Bristol, BS8 1TR Bristol, UK
[d] KU Leuven, Campus Diepenbeek, Mechanical Engineering Technology, Wetenschapspark 27, 3590 Diepenbeek
[e] Institute of Fundamental Technological Research, Polish Academy of Sciences, Pawinskiego 5B, 02-106 Warsaw, Poland
[f] Dynamics and Control Research Group (DCRG), University of Bristol, BS8 1TR Bristol, UK

Abstract

This paper investigates the mechanisms that can be used to enhance the absorption performance of poro-elastic materials in the viscous regime. It is shown that by adding small inclusions in a poro-elastic foam layer, a mass-spring effect can be introduced. If the poro-elastic material has relatively high viscous losses in the frequency range of interest, the mass-spring effect can enhance the sound absorption of the foam by introducing an additional mode in the frame and increasing its out-of-phase movement with respect to the fluid part. Moreover, different effects such as the trapped mode effect, the modified-mode effect, and the mass-spring effect are differentiated by decomposing the absorption coefficient in terms of the three energy dissipation mechanisms (viscous, thermal, and structural losses) in poro-elastic materials. The physical and geometrical parameters that can amplify or decrease the mass-spring effect are discussed. Additionally, the influence of the incidence angle on the mass-spring effect is evaluated and a discussion on tuning the inclusion to different target frequencies is given.

Keywords: Meta-poro-elastic material, Biot-Allard poroelastic model, Mass-spring effect, Viscous regime

1. Introduction

Porous materials are widely used as acoustic absorbers. They are inefficient and bulky solutions at low frequencies since they only exhibit perfect or near perfect absorption at the so-called quarter-wavelength resonance frequency. Multi-layering is a well-known and traditional approach to improve the efficiency of porous materials at low frequencies, which is again limited by the allowable thickness [1]. Researchers

Email address: sepide.ahsani@kuleuven.be (S. Ahsani)

have recently addressed this issue using unconventional solutions, such as embedding inclusions in the foam to create macroscopically inhomogeneous porous materials. Groby et al. [2] investigated the effect of low/high contrast inclusions in terms of both modal behavior and the acoustic response. They showed that, by considering a high contrast inclusion, the modified mode of the porous layer can be induced, leading to an increase in the absorption. The modified mode of the porous layer is defined as modes with evanescent waves in the ambient fluid and propagative waves in the porous layer, hence leading to energy entrapment in the porous layer. Moreover, they showed that the modified mode frequency has a positive frequency offset with respect to the natural frequency of the homogeneous layer. This frequency offset is dependent on the periodicity length and the inclusion dimension. Later on, Groby et al. [3] used periodic rigid inclusions to improve the absorption of a rigid-frame foam layer under the quarter-wavelength limit. They demonstrated that if the size of the inclusion is comparable to the acoustic wavelength, energy can be trapped between the inclusion and the rigid backing, and therefore be dissipated through viscous and thermal effects. Moreover, they showed that perfect or near perfect absorption due to this trapped mode can be achieved above the decoupling frequency, i.e. in the inertial regime. Their findings led Lagarrigue et al. [4] to create a meta-porous layer using a periodic array of rigid split-ring resonators (analyzed in the air by Krynkin et al. [5]) which, when used as inclusions in a rigid-frame foam, improve the absorption by combining the trapped mode phenomena and the resonance of the fixed rigid split-ring resonators. Additionally, in Ref. [6] authors extended the idea to a 3D configuration by using Helmholtz resonators to enhance the absorption coefficient of a rigid-frame porous material in the inertial regime due to Helmholtz resonances and the trapped mode effect. In a more recent work, Weisser et al. [7] investigated the concept of a meta-poro-elastic system below the decoupling frequency. They considered two different types of elastic inclusions; a homogeneous and relatively stiff inclusion made of steel or plexiglass, and a thin-wall resonant shell inclusion filled with air, having a pronounced mode in the lower frequency regime. The stiffer inclusion, made of rubber, resulted in similar performance as a rigid inclusion in the rigid-frame foam layer [3]. The more flexible shell inclusion, however, led to additional absorption enhancement at low frequencies due to the flexural modes of the shell. Zieliński [8] investigated numerically the effect of introducing periodic point-mass inclusions in a poro-elastic layer. He showed that the absorption performance of poro-elastic materials can be improved by the so-called mass-spring effect, where the foam under the mass inclusions acts as a spring, creating a mass-spring system with a certain resonance frequency depending on the mass and location of the inclusion. This effect was shown experimentally in Ref. [9] in the context of transmission loss improvement when multiple mass inclusions were added to a foam layer. In view of exploiting frame vibrations, active meta-poro-elastic layers with piezoelectric inclusions were proposed by Zieliński in Ref. [10] to actively modify the vibrations of the elastic skeleton of the poro-elastic layer in order to increase sound absorption. This idea was further studied in Ref. [11], where small passive inclusions were added to enhance the active effect. Recently, the use of resonant behavior at the micro-scale to improve the acoustic performance of poro-elastic materials has been investigated and discussed in Refs. [12, 13], where micro-scale resonators are embedded in the pores of the poro-elastic material. These resonators consist of a cantilever beam with added mass at the tip. Lewińska et al. have demonstrated that the visco-thermal dissipation is increased by the local resonant effect and this is due to the complex coupling between the solid and fluid phase. Moreover, they have shown that the micro-resonators attenuate the fast compressional wave and that the amount of this attenuation depends on the pore size, the opening ratio (area fraction of the opening in the pores), and the viscosity of the fluid in the pores.

All the works mentioned above and many others like Refs. [14, 15, 16, 17, 18, 19] show great potential in meta-porous and meta-poro-elastic systems as an innovative solution to create narrow or broadband absorbers at low frequencies. However, the contributions were mainly focused on improving the absorption performance of foams with a low decoupling frequency and thus acting in the inertial regime. The current work focuses on improving the absorption performance of poro-elastic materials with a high decoupling frequency, for which the frame vibration cannot be neglected, by exploiting the resonant behavior induced by the mass-spring effect. Therefore, this paper investigates meta-poro-elastic systems with inclusions that are modeled under different assumptions, namely rigid and motionless, point-mass, and elastic, to distinguish the mechanisms that influence the acoustic response. With this gained knowledge, configurations can be designed that achieve absorption enhancement over a broader frequency range by combining these mechanisms. In this work, the Biot theory [20, 21] of poro-elastic materials is used to account for the frame's motion. Additionally, the criteria under which the mass-spring effect can be achieved are discussed in detail. Furthermore, a general guideline is given to tune the mass-spring absorption peak to a targeted frequency.

This paper is structured as follows. Section 2 explains the modeling technique used for the poro-elastic material and the inclusions. Section 3 includes three main parts. The first part discusses different structural resonant behaviors in meta-poro-elastic systems, while the second one dives deeper into the concept of the mass-spring effect. The third part concludes the section with a qualitative study on the tunability of the mass-spring effect.

2. Problem formulation

This section consists of four parts. The first part describes the problem configuration. The model used for the poro-elastic material is detailed in the second part. The third part explains the models used for the inclusion and the fourth part details the field variables representation in a periodic configuration.

2.1. Problem configuration

The cases studied in this paper, depicted in Figure 1, are assumed to be invariant in the $z-$direction. The studied cases include an acoustic domain (Ω_{a}), being the ambient fluid, and a poro-elastic domain (Ω_{p}) with a thickness L_y and a rigid backing on the bottom. The poro-elastic and acoustic domains are periodic in the $x-$direction with a unit cell characteristic length of L_x. The $x-$direction periodicity is accounted for by using periodic field variables, as described in Section 2.4. Moreover, meta-poro-elastic cases are considered by introducing a rod inclusion of radius r at the location of $(\frac{L_x}{2}, y)$. Additionally, the system is constrained in the $y-$direction at the base end and is impinged by a plane wave at the top end with an oblique incidence angle θ.

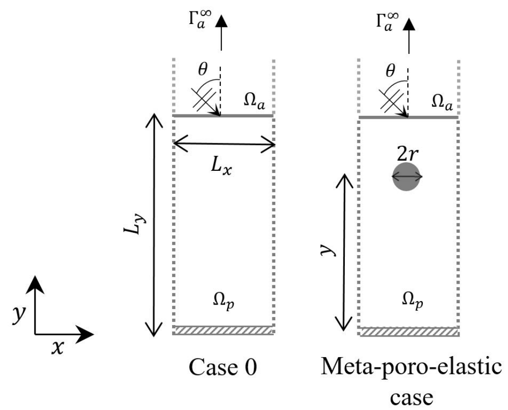

Figure 1: Schematic view of the cases considered in this paper.

2.2. Poro-elastic material modeling

The theory of Biot [20, 21, 22] is used to model the poro-elastic material such that the visco-elasticity and motion of the frame are taken into account. This is to ensure that viscous effects are correctly accounted for when analyzing the absorption behavior below the decoupling frequency.

The mixed $\mathbf{u}$-p formulation [23, 24] of the Biot poro-elasticity theory [20, 21, 25] is used, in which the primary field variables are the solid phase displacements $\mathbf{u}$ and the fluid pressure in the pores p. This formulation is valid for harmonic motion, and is described by the following set of coupled solid and fluid phase equations of motion:

$$\nabla \cdot \boldsymbol{\sigma}(\mathbf{u}) + \omega^2 \tilde{\rho}\, \mathbf{u} + \tilde{\gamma}\, \nabla p = \mathbf{0}, \tag{1}$$

$$\nabla^2 p + \omega^2 \frac{\tilde{\rho}_{22}}{\tilde{R}} p - \omega^2 \tilde{\gamma}\, \frac{\tilde{\rho}_{22}}{\phi^2} \nabla \cdot \mathbf{u} = 0, \tag{2}$$

with

$$\tilde{\rho} = \tilde{\rho}_{11} - \frac{\tilde{\rho}_{12}^2}{\tilde{\rho}_{22}}, \qquad \tilde{\gamma} = \phi \left(\frac{\tilde{\rho}_{12}}{\tilde{\rho}_{22}} - \frac{\tilde{Q}}{\tilde{R}} \right). \tag{3}$$

Here, ϕ is the porosity, while $\tilde{\rho}_{11}, \tilde{\rho}_{22}$, and $\tilde{\rho}_{12}$ are the effective densities which take into account the fact that the relative flow through the pores is not uniform and that there is a visco-inertial interaction between the solid and fluid phases leading to energy dissipation induced by the relative motion of the two phases [23, 26]. Furthermore, $\tilde{Q}$ is a coupling coefficient between the dilatation and stress of the two phases, while $\tilde{R}$ is the bulk modulus of the fluid phase. The second-order tensor $\boldsymbol{\sigma}(\mathbf{u})$, which appears in the solid phase equation of motion (1), describes the stresses in the elastic frame in vacuum and depends only on the solid phase displacement, namely,

$$\boldsymbol{\sigma} = \hat{A}\, (\nabla \cdot \mathbf{u})\, \mathbf{I} + \tilde{N} \left(\nabla \mathbf{u} + \nabla^{\mathrm{T}} \mathbf{u} \right), \tag{4}$$

where $\mathbf{I}$ is the second-order identity tensor, while $\hat{A}$ and $\tilde{N}$ are the Lamé coefficients of the visco-elastic frame. When ν, N, and η denote the bulk Poisson ratio, shear modulus, and loss factor of the frame, respectively, then: $\tilde{N} = N(1 + \mathrm{i}\eta)$ and $\hat{A} = \frac{2\nu}{1-2\nu} \tilde{N}$. Note that both these coefficients are complex-valued because of the visco-elastic behaviour of the frame leading to structural energy losses.

The formulae for the effective densities $\tilde{\rho}_{11}, \tilde{\rho}_{22}$, and $\tilde{\rho}_{12}$ can be found, for example, in Refs. [22, 23, 27]. They depend not only on the (homogenised bulk) densities of solid and fluid phases but also on a frequency-dependent viscous damping coefficient [22, 27]:

$$\tilde{b} = \mathrm{i}\omega\, \phi \rho_{\mathrm{a}} \left(\tilde{\alpha}(\omega) - \alpha_\infty \right), \tag{5}$$

which accounts for viscous interaction forces. This coefficient is related to the fluid phase density $\phi\rho_{\mathrm{a}}$ (here, ρ_{a} is the density of air, i.e. the actual fluid in pores) and to the difference between the frequency-dependent viscous dynamic tortuosity $\tilde{\alpha}(\omega)$ and kinematic tortuosity α_∞ of the porous material. Johnson et al. [28] proposed a semi-phenomenological model for $\tilde{\alpha}(\omega)$ depending on the transport parameters of porous material, viz. the viscous permeability (or airflow resistivity σ), porosity ϕ, kinematic tortuosity α_∞, and viscous characteristic length Λ. The effective moduli $\tilde{Q}$ and $\tilde{R}$ can be computed from formulae provided in [25, 22, 23, 24]. In particular, they depend on the dynamic (i.e. frequency-dependent) effective bulk modulus of air-saturated rigid porous medium for which a semi-phenomenological model was proposed by Champoux and Allard [29]. In that way, the Biot-Allard model [22, 27, 28, 29] for sound propagation and absorption in poro-elastic materials is applied in this work for all analyses assuming a visco-elastic frame, while the Johnson-Champoux-Allard (JCA) equivalent-fluid model [22, 28, 27] is occasionally used for comparison when the frame is assumed rigid.

2.3. Inclusion modeling

In this paper, three different ways are used to model the inclusion in order to isolate different effects, i.e. the mass-spring effect, the trapped mode effect, and the effect of the modified mode of the frame, leading to an increase in the absorption coefficient in dedicated frequency ranges.

2.3.1. Point- mass inclusion

The first and the most simple approach is to consider the inclusion as a concentrated mass (m_0), distinguishing the mass-spring effect from the others. Therefore, an inertial weak contribution is added to the variational formulation of the poro-elastic material [8]:

$$\mathcal{WF}_{\mathrm{p}} + \int_{\Omega_p} \omega^2 m_0 \, \delta(\mathbf{x} - \mathbf{x}_0) \, \mathbf{u} \cdot \mathbf{w} \, d\Omega_p = 0. \tag{6}$$

$\mathcal{WF}_{\mathrm{p}}$ is the weak form for a poro-elastic material in the domain Ω_p, m_0 is the point-mass of the inclusion concentrated at the point $\mathbf{x}_0$, δ is the Dirac delta function, and $\mathbf{w}$ is the test function for $\mathbf{u}$.

2.3.2. Rigid and motionless inclusion

In the second approach, to exclude the effect due to the motion of the inclusion (resonance behaviour), and therefore, to identify the effect induced by the inclusion size and geometry (trapped mode effect and modified mode of the frame), the inclusion of finite size is simply considered rigid and motionless. To model this, boundary conditions for a rigid and impervious wall are applied on the inclusion surface $\Gamma_{\text{p-r}}$, which means that the solid phase displacements and normal displacements of the fluid phase are zero on $\Gamma_{\text{p-r}}$ [30, 24]. Since the second condition (which describes the fact that there is no relative mass flux across the impervious boundary) is naturally handled in the enhanced $\mathbf{u}$-p formulation [24] (i.e. the corresponding surface integral in the weak formulation is zero), only the kinematic condition for the solid phase displacements [24], i.e. $\mathbf{u} = \mathbf{0}$ on $\Gamma_{\text{p-r}}$, needs to be included.

2.3.3. *Elastic inclusion*

In the third approach, the coupling between different effects (inertial, trapped mode effect, and modified mode of the frame) is taken into account by modeling the inclusion as an isotropic elastic domain and assuming that the poro-elastic layer is glued to the surface of this domain. Therefore, coupling conditions are applied on the interface $\Gamma_{\text{p-e}}$ between the poro-elastic and elastic domains, namely [30, 24]: the continuity of the total normal stresses at the interface, no relative mass flux across the impervious interface, and the continuity of the solid phase displacement vector of poro-elastic medium $\mathbf{u}$ and the elastic displacement vector $\mathbf{u}^{\text{e}}$ of the inclusion. However, since in the $\mathbf{u}$-p formulation the coupling between the poro-elastic and elastic media is natural, only the kinematic coupling condition, i.e. $\mathbf{u} = \mathbf{u}^{\text{e}}$ on $\Gamma_{\text{p-e}}$, has to be explicitly imposed [24].

2.4. *Field representations*

As the problem is periodic in space and is excited by a plane wave, the field variables are considered to be periodic (in the x-direction) in the poro-elastic domain Ω_{p}, acoustic domain Ω_{a}, and elastic domain Ω_{e}. Therefore, each field variable W satisfies the Floquet-Bloch relation [31]:

$$W(\mathbf{x} + \mathbf{d}) = W(\mathbf{x}) \exp(\mathrm{i}\tilde{\mathbf{k}} \cdot \mathbf{d}), \tag{7}$$

where $\mathbf{d}$ is the spatial periodicity and $\tilde{\mathbf{k}} = \{\tilde{k}_1, \tilde{k}_2, 0\}$ is the in-plane component of the incident wave number. In our case $\mathbf{d} = \{d_1, 0, 0\}$, where $d_1 = L_x$. Then, the periodicity in solid, acoustic, and poro-elastic domains can be taken into account by substituting the field variables W in the governing equations of each domain by their periodic generalisations [32] $\hat{W}(\mathbf{x}) = W(\mathbf{x}, \tilde{\mathbf{k}}) \exp(\mathrm{i}\tilde{\mathbf{k}} \cdot \mathbf{x})$. The corresponding weak forms associated with the dynamic equations of each domain are given in Appendix A. Moreover, the mutual interaction between the acoustic and poro-elastic domains is ensured in two steps [30]. In the first step, the continuity of the pressure at the interface of the two domains is applied. In the second step, the pressure in the acoustic domain at the interface is considered as a surface traction force on the solid phase of the poro-elastic domain, while the structural acceleration due to the solid phase of the poro-elastic domain is applied on the acoustic domain pressure. Readers are referred to [33] for the mathematical expression of the acoustic-poro-elastic coupling condition. Furthermore, the radiating boundary condition is applied by using the Floquet mode decomposition, as explained in [31].

3. Results and discussion

This section is divided into three main parts. In the first part, the discussion focuses on the resonant behaviors, namely the mass-spring resonance and the frame resonance in meta-poro-elastic materials, by investigating three cases. The differences between the modified mode and the mass-spring effects are pointed out by analyzing the decomposed absorption coefficients in terms of three energy dissipation mechanisms, i.e. viscous, thermal, and structural losses [27]. In the second part, the mass-spring effect is studied in detail. The investigation is mainly focused on the conditions under which the mass-spring effect is amplified or disappears. These limits are evaluated, taking into account the inclusion mass and size, as well as the poro-elastic material properties. In the third part, an optimization routine is used to derive optimum values for geometrical parameters of the inclusion such that the mass-spring effect is obtained at a specified frequency. The evolution of these parameters over frequency is then analyzed to derive a qualitative guideline to design a meta-poro-elastic material for a targeted frequency.

3.1. Resonant behavior in poro-elastic materials

This section investigates the induced resonant behaviors in the poro-elastic skeleton due to the added inclusions and how they improve the absorption performance. Two resonant behaviors are studied: the modified mode of the frame and the mass-spring effect. The former refers to the first mode of the frame and how the vibration pattern and occurring frequency are influenced by the periodicity introduced in the system and the added stiffness/mass by the inclusion. The latter is a new mode of the system due to the mass of the inclusion which is resonating on the stiffness of the poro-elastic frame, hence constituting a mass-spring system.

The resonant behavior in the poro-elastic material is studied by considering three cases. The first case is the reference case (case 0) and is composed of a homogeneous (i.e. without inclusions) foam layer with a thickness of $L_y = 24$ mm set on a rigid backing. In the second and third cases, a steel rod inclusion with a radius of $r = 0.4$ mm is introduced at $y_A = 4$ mm (case A) and $y_B = 20$ mm (case B) from the rigid backing respectively. In both of these cases, the width of the periodic cell is $L_x = 8$ mm, which is the distance along the x-axis between the periodically embedded inclusions. In all analyses, Biot's poro-elasticity theory is used to model the poro-elastic foam, where the Johnson-Champoux-Allard (JCA) [22, 28, 29] model is used to determine the effective density and bulk modulus for the air saturating the pores. The required Biot-JCA parameters used in all analyses are those for a polyurethane foam given in Table 1, where N, η are the shear modulus and loss factor of the frame, ν is the bulk Poisson ratio, ρ_1 is the bulk density, ϕ is the porosity, α_∞ is the tortuosity, Λ, Λ' are the viscous and thermal characteristic lengths, and σ is the airflow resistivity. These parameters are taken from Ref. [23]. Note also that the transport parameters ϕ, α_∞, Λ, Λ', and σ are used by the JCA model of equivalent fluid when (for comparison) the foam is modeled as a rigid-frame porous material.

N (kPa)	η	ν	ρ_1 (kg/m^3)	ϕ	α_∞	Λ (μm)	Λ' (μm)	σ (Pa·s/m^4)
55	0.055	0.3	31	0.97	2.52	37	119	87000

Table 1: The Biot parameters of the foam [23]

COMSOL Multiphysics is used to discretize and solve the Finite Element (FE) analyses for each case. These problems have been implemented using the weak formulations given in Appendix A. Mesh convergence studies have been performed for all cases resulting in FE meshes consisting of 893, 1006, and 1275 quadratic elements, yielding 6126, 10197, and 14751 DOFs, for the meta-poro-elastic system with the rigid inclusion model, point-mass inclusion model, and elastic inclusion model, respectively.

3.1.1. Sound absorption of the homogeneous poro-elastic layer

The total sound absorption and the corresponding decomposed absorption coefficients for case 0, with normal angle of incidence, are shown in Figure 2. It can be seen that simultaneously a dip in total absorption and viscous losses, as well as a peak in the structural losses, appear at approximately 820 Hz. This frequency corresponds to the resonance frequency of the frame with rigid backing [22], which is calculated as follows:

$$f_r = \frac{1}{4L_y}\sqrt{\frac{K_c}{\rho_1}}, \tag{8}$$

where $K_c = \frac{2(1-\nu)N}{(1-2\nu)}$. Since the structural losses directly correspond to the amount of strain in the solid phase of poro-elastic material, the structural loss at the resonance frequency of the frame is increased. However, viscous losses depend on the viscous coupling coefficient, which is dependent on foam properties, and the out-of-phase movement of the fluid and solid phase. The latter explains the dip at f_r (in-phase movement of the fluid in the pores and the frame), and also the peak above f_r (anti-phase displacement of the frame and the fluid).

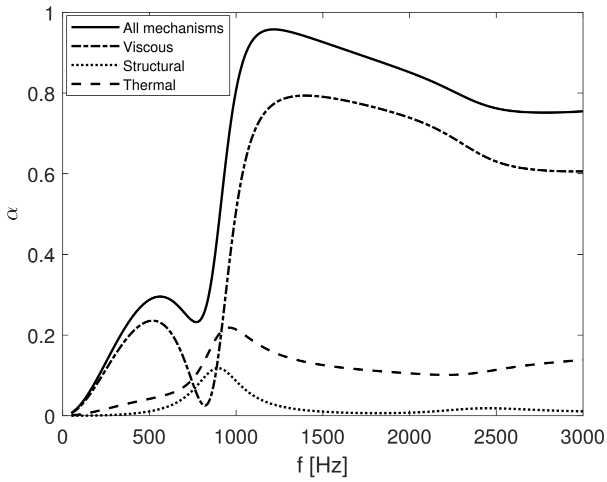

Figure 2: Partial absorption coefficient for different dissipation mechanisms for the poro-elastic foam without inclusions.

Another important characteristic of poro-elastic materials is the decoupling frequency f_c, at which the transition from viscous to inertial regime occurs. The harmonic motion of the fluid phase does not excite the frame above this frequency [22], i.e. the two phases are decoupled and the energy is dissipated mainly due to the inertial effect as opposed to the viscous drag between the two phases. The decoupling frequency is commonly defined as follows [21]:

$$f_c = \frac{\phi\,\sigma}{2\pi\rho_{\mathrm{a}}}, \tag{9}$$

where ρ_{a} is the density of air. It should be noted that above this frequency, the rigid frame assumption is valid and therefore the equivalent fluid model predicts the behavior of the poro-elastic layer with good accuracy. Even below f_c, for poro-elastic materials with sufficiently stiff (rigid) skeleton, no significant vibrations will be induced in the skeleton by airborne acoustic waves.

It is worth mentioning that other criteria can be used to identify the decoupling frequency such as the inverse quality factor [34] in the case of foams with very low viscous characteristic length. The decoupling frequency for the type of foam we are targeting (foams with a high value of flow resistivity) is at high frequencies, more specifically for the foam used in this work the decoupling frequency is at 11.2 kHz. Therefore, there is a significant deviation of the equivalent fluid model with respect to the theory of Biot in the studied frequency range, see Figure 3.

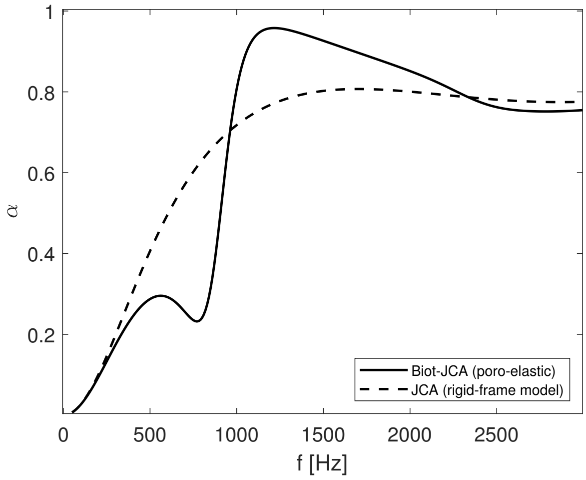

Figure 3: Absorption coefficients calculated for the homogeneous poro-elastic layer using the Biot-JCA (i.e. Biot-Allard) model and for the corresponding rigid-frame porous layer calculated using the JCA model of equivalent fluid.

3.1.2. Sound absorption of meta-poro-elastic systems in case of normal incidence angle

In this part, the (partial) absorption coefficients of case A and case B are calculated considering the three different modeling techniques detailed in Section 2.3 to distinguish different resonant behaviors, i.e. the mass-spring and modified mode effects. Below, the results corresponding to the different ways to model the inclusion are discussed, i.e. first for case A and then for case B. Afterward, the resonant behaviors induced in case A and case B due to the mass-spring system are compared to each other. These results are depicted in Figure 4. Moreover, the absorption coefficient of case 0 is recalled for comparison to have a view on the effect of inclusion on the acoustic response.

I. Different inclusion modeling techniques: Case A

The results are discussed in two steps. The first step considers the absorption coefficient corresponding to the model that assumes a motionless inclusion. The second step explains the results that take into account the inclusion motion.

- *Rigid and motionless inclusion model* It can be seen that the absorption coefficient obtained using the rigid and motionless inclusion model is almost identical to the one obtained for case 0 (cf. Figure 4 (a)) with a slight shift of the resonance frequency of the frame to a higher frequency (i.e. from 820 Hz to 910 Hz). This indicates that the rigid and motionless inclusion stiffens the skeleton, causing the first mode of the frame to be shifted upwards in frequency. The stiffening of the foam is due to the

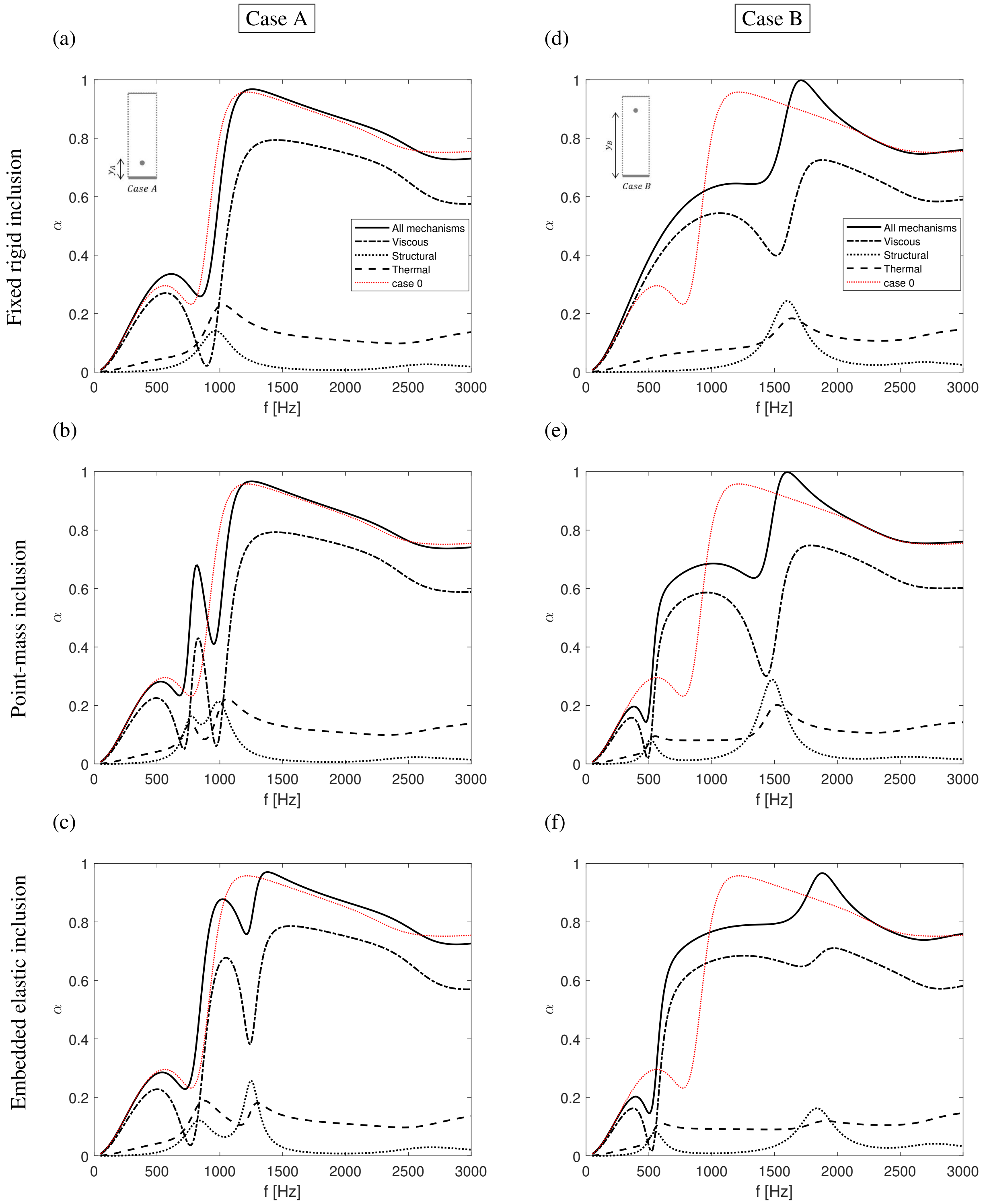

Figure 4: Total and partial absorption coefficients for case A (a,b,c) and case B (d,e,f), related to different dissipation mechanisms in the poro-elastic layer with the inclusion modeled as rigid (a,d), point mass (b,e) or elastic (c,f).

fact that the inclusion is modeled only by constraining the foam, and since the fixed rigid inclusion is located very close to the rigid backing, it results in an extended area of rigid-like boundary condition.

- *Point-mass and elastic model* The same observation does not hold for the point-mass inclusion (see Figure 4(b)) or the elastic inclusion (see Figure 4(c)), as there is clearly an additional peak in the absorption coefficient. This peak is lower in frequency and is more localised in the point-mass model as compared to the elastic inclusion model since in the point-mass model only the inertial effect is considered while the elastic model also accounts for the size effect. Additionally, we would like to draw the reader's attention to the two peaks in structural losses (see Figure 4(b),(c)), which indicate two resonance frequencies in the system. These peaks are at 770 Hz and 980 Hz for the point-mass inclusion, and they are at 840 Hz and 1250 Hz for the elastic inclusion. To identify the mass-spring resonance and the modified mode, the real part of the vertical component of the fluid and solid displacements (v and v^f) of case A with point-mass inclusion are evaluated at the frequencies of the total absorption peaks induced by the out-of-phase motion excited after the two structural loss peaks, see Figure 5. The vibration pattern of the frame at 820 Hz clearly presents a localized motion around the inclusion, while at 1250 Hz a modeshape of the skeleton modified due to the presence of the inclusion addition is noticeable. This indicates that the first structural loss peak is induced by the mass-spring resonance.

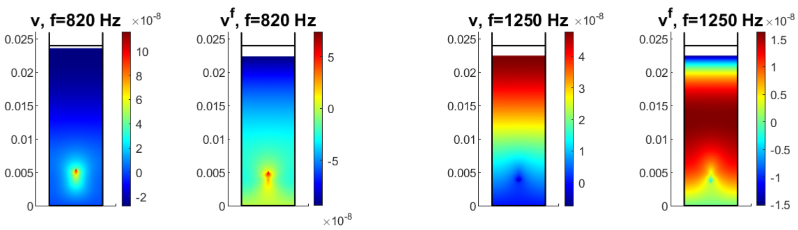

Figure 5: The displacement field (with v referring to the solid displacement along $y-$axis and v^f referring to the fluid displacement in the same direction) of case A with point-mass inclusion at $f = 820$ Hz (left), and $f = 1250$ Hz (right). These frequencies refer to the peaks in the total absorption coefficient after the mass-spring and frame resonances, respectively.

II. Different inclusion modeling techniques: Case B

The acoustic response related to different inclusion models is discussed for case B in the same manner as for case A.

- *Rigid and motionless inclusion model* As it is observable from Figure 4, the results obtained using the model with fixed (i.e. motionless) rigid inclusion differ significantly from those of case 0 because the longer distance between the inclusion and the rigid backing (as compared to case A) leads to a shift in the frame resonance frequency to higher frequencies. Therefore, the peak appearing in the total absorption and the partial structural absorption for the case with fixed rigid inclusion is simply due to the modification of the mode of the frame.

- *Point-mass and elastic model* For these models, a similar behavior (as in case A) is observed in case B. Specifically, the point-mass and elastic inclusion models both exhibit two peaks in structural losses resulting from the mass-spring system and the modified mode of the frame, respectively. Again, this can be confirmed by visualizing the displacement fields at the total absorption peaks induced by these effects and comparing them to each other, see Figure 6.

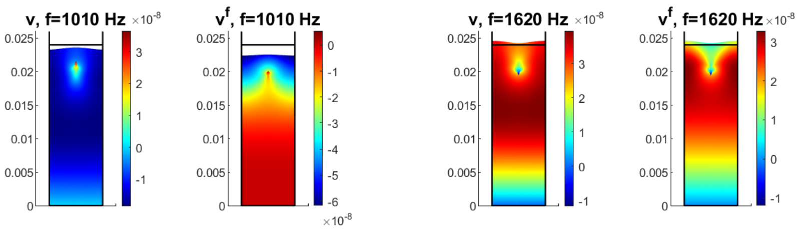

Figure 6: The displacement (with v referring to the solid displacement along $y-$axis and v^f referring to the fluid displacement in the same direction) of case B with point mass inclusion at $f = 1010$ Hz (left), and $f = 1620$ Hz (right). These frequencies refer to the peak in the total absorption coefficient after the mass-spring and frame resonance.

On the one hand, the absorption enhancement for case B is achieved over a broader frequency band as compared to case A for both the embedded elastic and point-mass inclusions due to the combined mass-spring and modified mode effects. On the other hand, the resonance frequency of the frame is shifted to higher frequencies as compared to case A and case 0 and the system reaches a perfect or almost perfect absorption at higher frequencies. As a result, the absorption coefficient is reduced at some higher frequencies in the meta-poro-elastic system as compared to case 0. For example, the maximum absorption for case 0 is 0.95 at 1140 Hz and is reduced at this frequency to 0.78 when an elastic inclusion is added, cf. Figure4(f).

III. Comparison of mass-spring resonance in case A and case B

When comparing the resonance frequency of the point-mass or elastic inclusion of case A to case B, it can be seen that by increasing the distance between the inclusion and the rigid backing that the peak is shifted down in frequency. This behavior can be explained by considering the foam under the inclusion as a spring. Therefore, increasing its length leads to a decrease in its stiffness, which results in a lower resonance frequency of the mass-spring system.

3.1.3. Sound absorption of meta-poro-elastic systems under oblique incidence angle

To assess the utility of the meta-poro-elastic system in real applications, the performance of the considered meta-poro-elastic configurations under oblique incidence angle is evaluated. Figure 7 shows the (partial) absorption coefficients calculated for case A and case B under different angles of incidence (θ) varying from 0°, i.e. normal incidence, to 78°, i.e. close to grazing incidence.

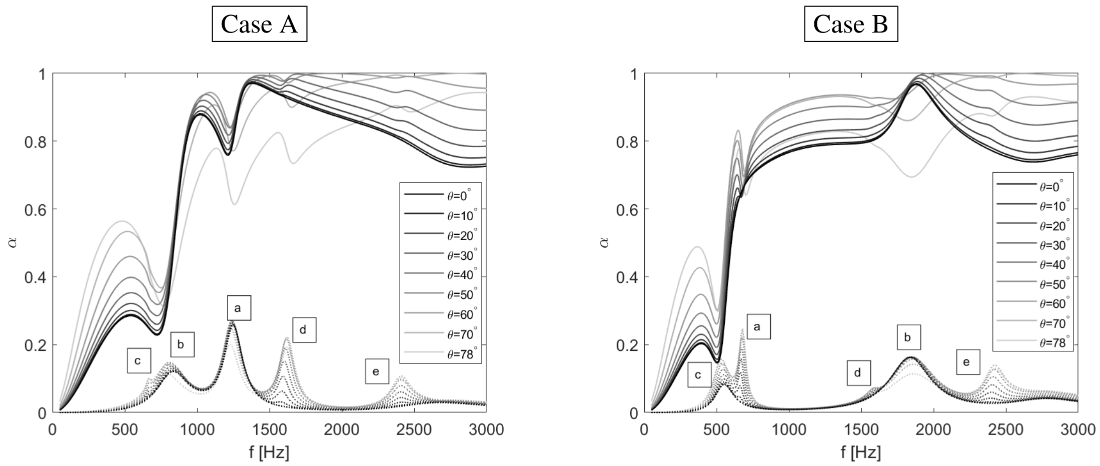

Figure 7: The total absorption coefficient (solid lines) and the partial structural absorption coefficient (dotted lines) of case A and case B with elastic inclusions under oblique incidence angle (θ).

As compared to normal incidence (Figure 4), the absorption curves under oblique incidence (Figure 7) show three additional peaks in the structural losses (labeled as c, d, and e in Figure 7) when the incidence angle deviates from $\theta = 0°$. Recall that the peaks marked with letters a and b correspond to the mass-spring effect and the modified mode effect along the $y-$axis, respectively. The additional peaks are related to the modes excited along the $x-$axis by the in-plane component of the incident plane wave. Two of which, i.e. c and d, are the modified first- and second-order shear modes due to inclusion, while the other one, i.e. e, is an additional mode excited by the inclusion resonating along the $x-$axis. The latter has a resonance frequency around 2400 Hz, which is double of the vertical mass-spring resonance for case A around 1250 Hz. This is because the horizontal distance of the inclusion (L_x = 8 mm) is double the vertical distance of the inclusion from the rigid wall for case A (y_A = 4 mm).

To assess the performance of case A and case B (with elastic inclusions) with respect to case 0 in a more general setting, the diffuse-field absorption of the two cases are compared to case 0 in Figure 8. This evaluation confirms that the mass-spring effect is preserved under the assumption of diffuse-field.

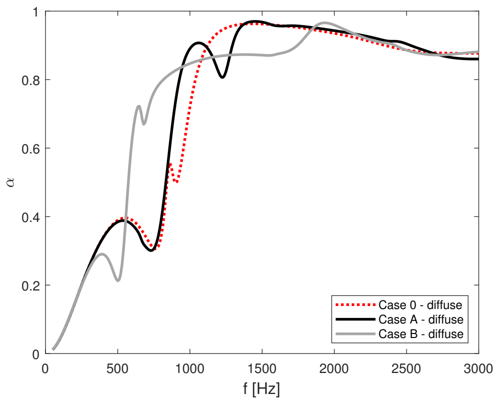

Figure 8: Diffuse-field absorption coefficient of case 0, case A, and case B.

3.2. *Mass-spring effect*

The previous part demonstrated that resonant behavior in a meta-poro-elastic system can lead to an absorption peak, whether it is by alternating the frame vibration pattern at its first natural frequency or by inducing an additional mode in the system, such as the mass-spring effect. This part investigates the conditions under which this mass-spring resonance leads to absorption improvement.

3.2.1. *Dependency on viscous transport parameters*

The mass-spring effect leads to an increase in the absorption coefficient by forcing the poro-elastic skeleton to move out-of-phase with respect to the fluid part due to the resonating inclusion. A larger phase difference results in an increase in viscous losses. Therefore, intuitively it is understood that the absorption coefficient enhancement due to the mass-spring effect strongly depends on the values of flow resistivity (σ) and viscous characteristic length (Λ). This statement is validated by considering case A and varying σ and Λ while keeping all the other parameters constant, and then plotting the absorption peak values due to the mass-spring effect (the local maxima in the absorption curve between the frequencies at which the two structural-loss peaks appear), see Figure 9(a). It is apparent in Figure 9(a) that the increase of absorption peak value is more sensitive to changes in the viscous characteristic length as compared to changes in the flow resistivity. Additionally, normalised values of the real part of the viscous coupling coefficient, i.e. $\mathrm{Re}(\tilde{b}/(\omega\rho_{\mathrm{a}}))$ see equation (5), are also calculated at those frequencies, and presented in Figure 6(b) for various values of σ and Λ. Recall that the viscous coupling coefficient (5) depends on the dynamic viscous tortuosity $\tilde{\alpha}$, which depends on σ and Λ according to the Johnson et al. [28, 22] model, and this coefficient corresponds to the amount of viscous losses. Note that $\mathrm{Re}(\tilde{b})$ is used for the plot in Figure 9(b) because the real part is associated with the dissipative part of the viscous forces, while the imaginary part $\mathrm{Im}(\tilde{b})$ is associated with the modification of tortuosity due to the added mass effect related to the viscous behaviour of the fluid in the pores [27]. From the graphs in Figure 9, it can be seen that the mass-spring effect can occur in all types of poro-elastic foams, but that pronounced improvements in absorption only occur in foams with high flow resistivity and/or low viscous characteristic length (cf. white and light-gray areas in Figure 9).

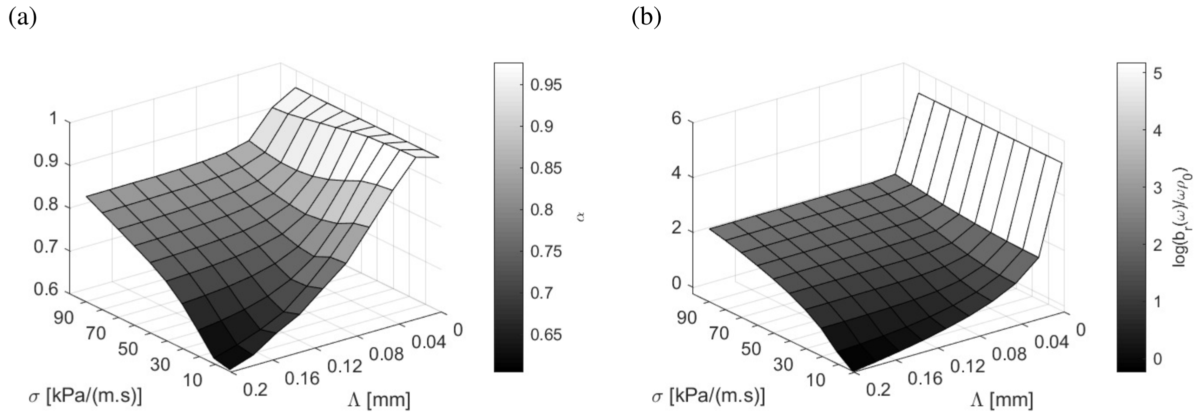

Figure 9: The value of the absorption coefficient peak due to the mass-spring effect (a) and the value of normalised viscous coupling coefficient at the absorption peak frequencies (b) for different combinations of viscous characteristic length and flow resistivity.

3.2.2. Dependency on inclusion properties

The size and mass of the inclusion impact both the total absorption coefficient and the mass-spring effect. To verify their effect, an investigation is carried out in three steps. In the first step, the effect of the inclusion mass is investigated by keeping the size of the inclusion constant (r = 0.4 mm) and increasing its mass density. In the second step, in order isolate the effect of inclusion size the inclusion mass is kept constant and equal to that of a steel rod of radius r = 0.4 mm, while the inclusion size is increased. In the third step, the combined effect of size and mass is evaluated by increasing the elastic inclusion size.

I. *The effect of inclusion mass*

In the first step, the effect of the inclusion mass is investigated by considering the elastic inclusion of case A and case B and increasing its mass density such that the inclusion mass (m) is equal to the mass (m_r) of a steel rod with radius $r_{eq} = 0.2, 0.4, 0.8, 1.2, \ldots, 3.6$ mm, while keeping the inclusion size constant and equal to $r = 0.4$ mm. The total absorption coefficients, as well as the partial absorption coefficients due to structural losses, are compared in Figure 10 for the considered values of the inclusion mass. Additionally, the blue line in Figure 10 is the projection of the first structural losses peak on the $f - r_{eq}$ plane. Similarly, the red line is the projection of the second absorption peak on the $f - r_{eq}$ plane. Moreover, the red and blue dots are the values of total absorption at these structural peaks.

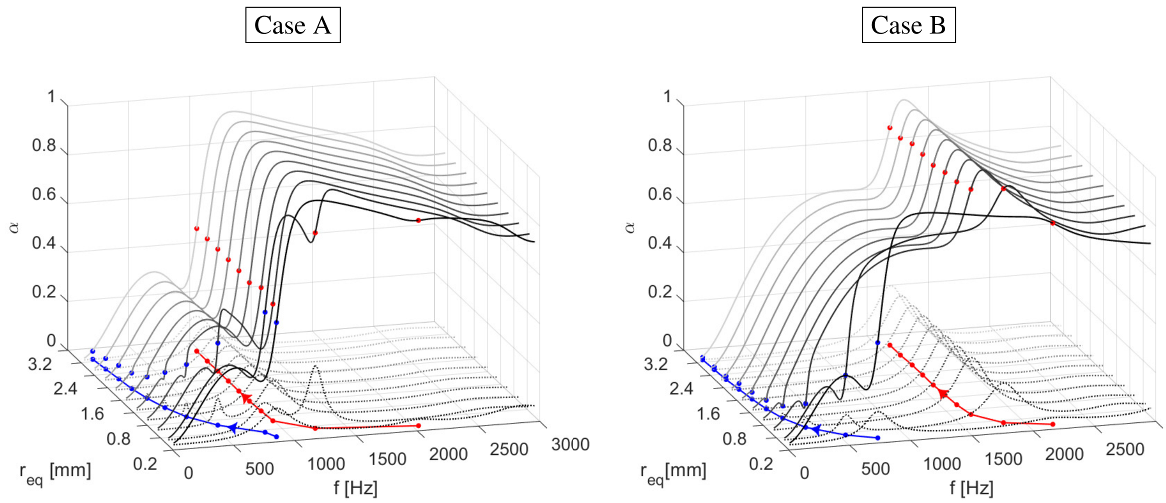

Figure 10: The total absorption (black and gray continuous curves) and partial absorption due to structural losses (black and gray dotted curves) for poro-elastic cells containing an elastic rod inclusion with the same radius $r = 0.4$ mm and various masses (m) equivalent to the mass (m_r) of an inclusion with a radius of $r = r_{eq}$ in millimeter.

Considering both cases, it is clear that both the mass-spring resonance frequency (the blue line) and the resonance frequency of the frame (the red line) are shifted down in frequency when the inclusion mass is increased. For both cases, above a certain amount of mass addition (i.e. $m_{1.6}$), the observed behavior converges asymptotically as the mass increases. This means that the mass-spring resonance frequency converges to zero for heavy inclusions, and the inclusion only modifies the mode of frame. Moreover, the value of the peak in structural losses due to inclusion resonance decreases as it is shifted down in frequency since at lower frequencies fewer cycles per second occur and hence less energy is dissipated.

II. *The effect of inclusion size*

The influence of different inclusions sizes, while keeping mass fixed, is shown in Figure 11. It can be seen that the resonance frequency of the inclusion (the blue curve), increases for larger inclusion sizes, and hence follows the opposite trend as for the previous study illustrated in Figure 10. This is explained by the fact that increasing the size of inclusion leads to an increase in the effective area of the spring and a decrease in the effective length of the spring [35]; thus, the spring stiffness is increased while the mass remains the same which increases the mass-spring resonance frequency. Similarly, the resonance frequency of the frame (the red curve) is also shifted up in frequency. The shift in resonance frequency of the frame is due to the added stiffness to the frame in combination with a decrease in the distance between the inclusion and the rigid backing as the inclusion dimension increases, which leads to an extended area of rigid-like boundary condition on the foam and thus increasing the frame resonance frequency.

It should be noted that in case B the total absorption coefficient drops significantly for larger inclusions. This occurs because the inclusion size becomes comparable to or larger than the two longitudinal wavelengths, i.e. $\frac{\lambda}{r} \approx 2$ for $r = 2.4$ mm at $f = 1500$ Hz, and it is located very close to the surface. Consequently, most of the wave is reflected. Additionally, the spacing between the inclusions decreases with the increase in the inclusion size (because the width of the periodic cell remains the same), leading to a decrease in the material that the sound wave can propagate through and be dissipated.

It can be seen that the peaks due to the mass-spring resonance are more pronounced for larger inclusions. This is related to the fact that when the size of the inclusion is increased, the added mass is distributed over a larger area, therefore it affects a wider area of the foam around it, i.e. increase in the frame displacement which corresponds to a higher peak in the structural loss. Additionally, the resonance frequency of the inclusion is shifted higher in frequency, where more cycles per second occur and hence more energy can be dissipated.

To demonstrate the former, the field variables (i.e. the solid phase displacements, the fluid phase displacements, and the pressure) at the inclusion resonance frequency (800 Hz) are shown for the smallest and the largest inclusions in Figure 12, where the real part of the solid displacement along the $x-$axis and along the $y-$axis, and the real part of the pore pressure are denoted by u, v, and p, respectively. The real part of the fluid displacement along the $x-$axis and along the $y-$axis are indicated with u^f and v^f, respectively. Figure 12 shows that at $f = 800$ Hz for both cases the frame is excited by the resonating inclusion to move out-of-phase with the fluid phase and it is clear that the area of the poro-elastic layer affected by the large

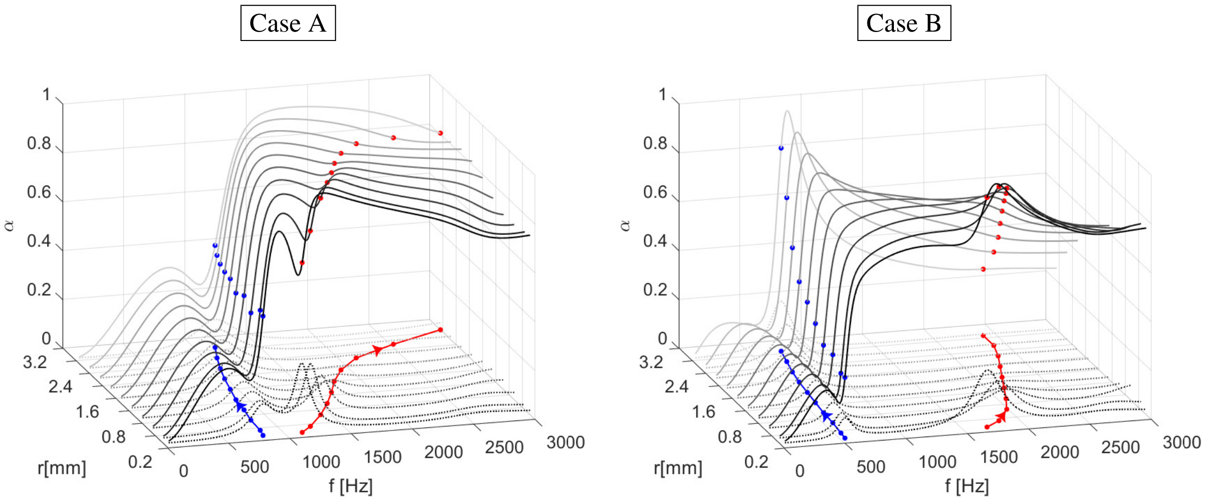

Figure 11: The total absorption (black and gray continuous curves) and partial absorption due to structural losses (black and gray dotted curves) for poro-elastic cells containing an elastic inclusion with various radii r, but constant mass equal to that of a steel rod with a radius 0.4 mm.

inclusion is larger than the area affected by the small inclusion.

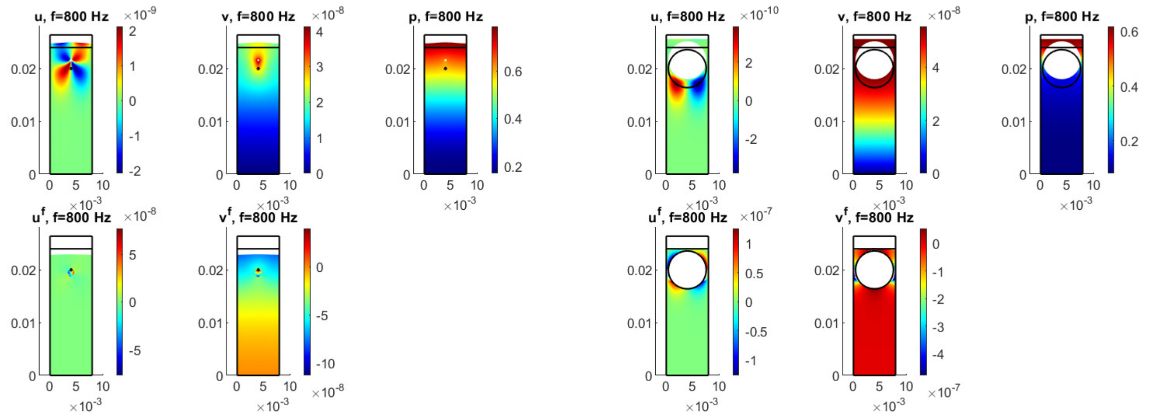

Figure 12: The field variables at $f = 800$ Hz in the poro-elastic layer with elastic inclusion with a radius of $r = 0.2$ mm (graphs on the left) or 3.6 mm (graphs on the right).

III. *The combined effect of the inclusion mass and size*

To conclude this study on the influence of geometry, the radius of, and accordingly the mass of, the steel inclusion is varied. The total absorption, as well as the partial absorption coefficients due to structural losses, are shown in Figure 13 for both cases A and B.

Considering case A it is apparent that by increasing the diameter of the inclusion, and consequently the added mass, the mass-spring resonance (the blue line) is shifted down in frequency (from 1920 Hz to

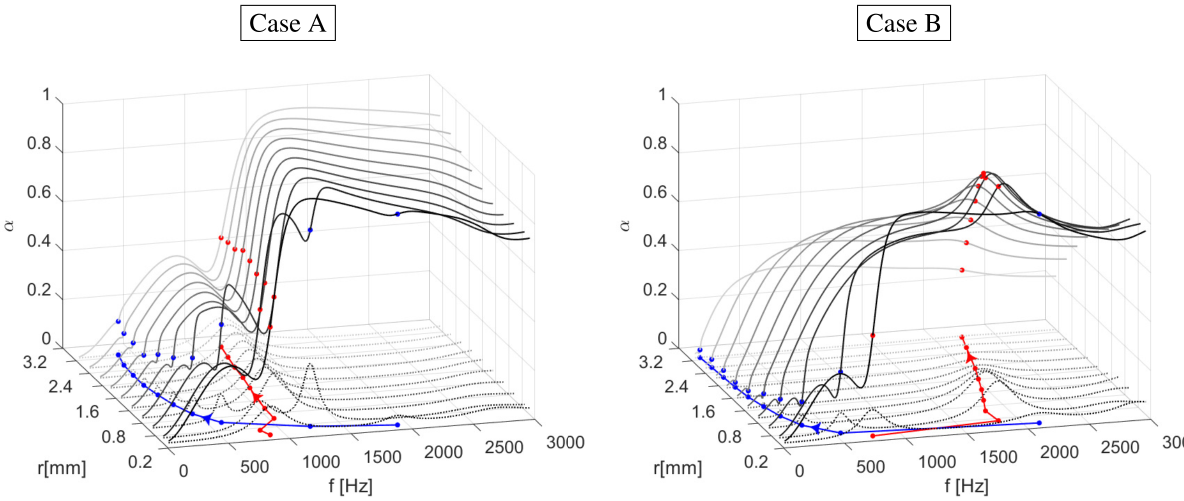

Figure 13: The total absorption (black and gray continuous curves) and partial absorption due to structural losses (black and gray dotted curves) for poro-elastic cells containing a steel rod inclusion of different radii.

320 Hz), while the resonance frequency of the frame (the red line) is shifted up in frequency (from 890 Hz to 1210 Hz). The value of the peak in structural losses due to the mass-spring resonance decreases since the larger inclusion rigidifies the foam and also in lower frequencies the energy dissipation decreases due to fewer cycles per second. It should be noted that the shift in resonance frequency of the mass-spring system is due to the increase in added mass, which is more dominant than the increase in the effective area and decrease in the effective length of the spring acting underneath the inclusion. The shift in the resonance frequency of the frame follows the same trend as in the previous study. For very small inclusions (i.e. $r = 0.2$ mm and $r = 0.4$ mm) the resonance frequency of the frame is lower than that of the inclusion (therefore, the red and blue curves intersect).

All remarks explained above can be observed more clearly in case B (Figure 13(right)) since the resonance frequency of the mass-spring system and frame are located further apart. In this case, the mass-spring resonance frequency lowers from 2100 Hz to 80 Hz, and at the same time the frame resonance frequency shifts up from 770 Hz to 2160 Hz.

3.3. Tunablity of the mass-spring effect

As a final study the combined effect of the inclusions size and location is investigated in order to find the optimal absorption that can be achieved at various frequencies. To do so, an optimization problem is defined with a design space consisting of the inclusion radius (r) and the vertical position of the inclusion (y). These parameters are optimized at each frequency such that a curve indicating the maximal achievable absorption is obtained. The following objective function is used:

$$f_p = |1 - \alpha|^2. \tag{10}$$

The presented optimization problem is solved using the *patternsearch* function in Matlab [36, 37]. It should be mentioned that the elastic inclusion model is used in the optimization problem.

Figure 14 summarizes the results of this optimization routine. The optimized parameter values at the targeted frequencies between 100 Hz and 3000 Hz are shown in Figure 14(b), while the best feasible absorption coefficient values, by using the optimized parameters at each frequency, are marked with red circles in Figure 14(a).

Two different trends in the design parameters progression over two frequency ranges are observed and marked in white in Figure 14(b). The first frequency range, from 500 Hz to 900 Hz, is the mass-spring dominated region, while the second one, from 1700 Hz to 3000 Hz, is dominated by the modified mode effect. In the first frequency range, the absorption enhancement is due to the mass-spring effect and the resonance frequency has a negative relation with the inclusion size and its (absolute) position from the rigid backing. Moreover, Figure 14(b) shows that (in this region) the size of the inclusion should be deep-subwavelength since there is a drop in inclusion size from sub-wavelength scale ($\frac{\lambda}{r} \approx 40$) to deep-subwavelength ($\frac{\lambda}{r} \approx 200$) at 500 Hz, where the mass-spring effect dominated region begins.

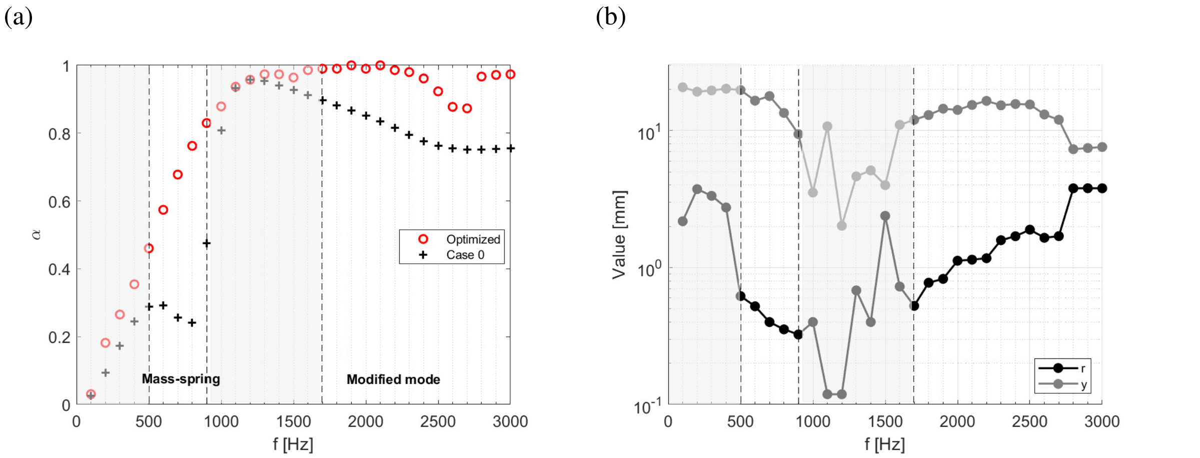

Figure 14: The absorption coefficient at the targeted frequencies of the optimization (a), and the converged values of the design space parameters (b). The red circles in the left plot refer to the best absorption coefficient value that can be obtained at each targeted frequency using the parameters shown in the right plot at that specific frequency.

In the second region, i.e. the modified mode dominated region, the frequency has a positive relation with the inclusion size. The reason for this is that the larger inclusion stiffens the foam and shifts the mode of the frame to a higher frequency. However, the optimal inclusion position does not seem to be strongly dependent on the frequency at which it is optimised and it seems that the optimal position of the inclusion is approximately in the middle of the foam layer for all the frequencies in the modified mode dominated region.

There is a transition zone between the two regions (the gray area from 900 Hz to 1600 Hz), where the choice of the design parameters seems to be more random. This zone starts around the natural mode of the frame in case 0, i.e. at $f_r \approx 820$ Hz. Inside this zone, the design parameters cannot be optimized because: (i) the inclusion is already at the lowest vertical position and lowest dimension possible, therefore the mass-spring effect has reached its limit; (ii) the modified mode is always higher in frequency as compared to the natural mode of the frame and there will be always a minimum frequency offset between them. This minimum frequency offset corresponds to unit cell characteristic length which is fixed in this case. All this results in a transition zone that is neither dominated by the mass-spring effect nor by the modified mode effect.

4. Conclusions

In this paper the absorption of poro-elastic material is enhanced in the viscous regime using a mass-spring effect. It is shown that by embedding a deep-subwavelength inclusion in a poro-elastic layer a mass-spring system can be induced, where the foam under the inclusion acts as a spring. Therefore, by tweaking the added mass and its distance from the rigid backing the resonance frequency of the system can be tuned. More specifically, the resonance frequency of the mass-spring system has an inverse relation with both of these parameters. Moreover, it is shown that the resonating inclusion excites the out-of-phase motion between the fluid and solid phase of the porous material leading to an increase in the energy dissipation due to viscous effects. This phenomenon is apparent for the poro-elastic material under the decoupling frequency and when the inclusion is fully coupled to the poro-elastic domain or at least modeled as a point-mass inclusion. The mass-spring effect is identified by decomposing the absorption coefficient in three energy dissipation mechanisms, viz. viscous, thermal, and structural, for three different cases of poro-elastic layers, namely, without inclusion and with inclusion at two different locations (i.e. close to the rigid backing or layer surface). It is shown that the peaks in the absorption curve correspond to the increase in out-of-phase movement of the two phases, which happens at the resonance frequency of the mass-spring system and the resonance frequency of the frame. This explains that the mass-spring effect increases the viscous energy dissipation by forcing the frame to move out-of-phase with the fluid part. After elaboration on the resonant behaviors in the proposed meta-poro-elastic systems, the physical and geometrical parameters that intensify or degrade the mass-spring effect were discussed. It was demonstrated that, since the mass-spring effect enhances the absorption coefficient through viscous losses, the poro-elastic layer should have a relatively high viscous energy dissipation at low frequencies. This translates into a high value of the flow resistivity and/or a low value of the viscous characteristic length. Additionally, it was shown that the size of the inclusion plays an important role in the effectiveness of the meta-poro-elastic system: when the inclusion size becomes comparable to the wavelength in the medium, the inclusion stiffens the foam around it leading to either extension of the rigid backing or reflection of the incidence wave from the surface by the large inclusion depending on its location. Finally, it is shown that the mass-spring effect increases the absorption coefficient in the viscous regime, even for an oblique angle of incidence. Therefore, this work presents the potential of this effect as an absorption enhancement strategy in poro-elastic materials with a high decoupling frequency.

Acknowledgements

The European Commission is gratefully acknowledged for their support of the VIPER research project (GA 675441). The Research Fund KU Leuven is gratefully acknowledged for its support. The research of E. Deckers is funded by a grant from the Research Foundation – Flanders (FWO). This research was partially supported by Flanders Make, the strategic research centre for the manufacturing industry. T. G. Zieliński and Ł. Jankowski would like to acknowledge the financial support from the National Science Centre (NCN), Poland, under Grant Agreement No. 2015/19/B/ST8/03979.

Appendix A. Weak forms

The weak integral formulation of the Helmholz equation for the acoustic pressure p inside the acoustic domain Ω_a reads:

$$-\int_{\Omega_\mathrm{a}} \frac{1}{\omega^2\rho_\mathrm{a}} \nabla\bar{q}\cdot\nabla p \,\mathrm{d}\Omega_\mathrm{a} + \int_{\Omega_\mathrm{a}} \frac{1}{K_\mathrm{a}} \bar{q} p \,\mathrm{d}\Omega_\mathrm{a} + \int_{\Gamma_\mathrm{a}} \frac{1}{\omega^2\rho_\mathrm{a}} \bar{q}\,\nabla p\cdot\mathbf{n}\,\mathrm{d}\Gamma_\mathrm{a} = 0, \tag{A.1}$$

where ρ_a and K_a are the density and bulk modulus of air, Γ_a is the Neumann-type boundary, $\mathbf{n}$ is the the outward unit vector to normal to it, while q and $\bar{q}$ are the test function for p and its complex conjugate. Considering a periodic solution to the problem of equation (A.1), the problem description can be reformulated as follows:

$$\mathcal{WF}_{\mathrm{a}} = -\int_{\Omega_{\mathrm{a}}} \frac{1}{\omega^2\rho_{\mathrm{a}}}\bar{\bar{\nabla}}\bar{\hat{q}} \cdot \hat{\nabla}\hat{p}\, \mathrm{d}\Omega_{\mathrm{a}} + \int_{\Omega_{\mathrm{a}}} \frac{1}{K_{\mathrm{a}}}\bar{\hat{q}}\hat{p}\, \mathrm{d}\Omega_{\mathrm{a}} + \int_{\Gamma_{\mathrm{a}}} \frac{1}{\omega^2\rho_{\mathrm{a}}}\bar{\hat{q}}\,\hat{\nabla}\hat{p} \cdot \mathbf{n}\, \mathrm{d}\Gamma_{\mathrm{a}} = 0, \tag{A.2}$$

where $\hat{p} = p\exp(\mathrm{i}\tilde{\mathbf{k}} \cdot \mathbf{x})$ and $\bar{\hat{q}} = \bar{q}\exp(-\mathrm{i}\tilde{\mathbf{k}} \cdot \mathbf{x})$ are the periodic pressure field and the corresponding test function. Here and below, $\bar{\hat{\nabla}} = \nabla - \mathrm{i}\tilde{\mathbf{k}}$ and $\bar{\nabla} = \nabla + \mathrm{i}\tilde{\mathbf{k}}$ are the shifted gradient operators for the test functions and field variables, respectively.

The weak formulation for the poro-elastic domain Ω_{p} can be reformulated in the same manner as for the acoustic domain by considering periodic representations $\hat{p}$ and $\hat{\mathbf{u}} = \mathbf{u}\exp(\mathrm{i}\tilde{\mathbf{k}} \cdot \mathbf{x})$ of the pore pressure p and solid phase displacements $\mathbf{u}$, respectively, namely:

$$\begin{aligned}\mathcal{WF}_{\mathrm{p}} = &\int_{\Omega_{\mathrm{p}}} \omega^2\tilde{\rho}\,\hat{\mathbf{u}} \cdot \bar{\hat{\mathbf{w}}}\, \mathrm{d}\Omega_{\mathrm{p}} - \int_{\Omega_{\mathrm{p}}} \hat{\boldsymbol{\sigma}}(\hat{\mathbf{u}}) \bullet \bar{\hat{\nabla}}\bar{\hat{\mathbf{w}}}\, \mathrm{d}\Omega_{\mathrm{p}} + \int_{\Omega_{\mathrm{p}}} \left(\tilde{\gamma} + \tilde{\xi}\right)\bar{\nabla}\hat{p} \cdot \bar{\hat{\mathbf{w}}}\, \mathrm{d}\Omega_{\mathrm{p}} + \int_{\Omega_{\mathrm{p}}} \tilde{\xi}\hat{p}\,\bar{\hat{\nabla}} \cdot \bar{\hat{\mathbf{w}}}\, \mathrm{d}\Omega_{\mathrm{p}}\\ &- \int_{\Omega_{\mathrm{p}}} \frac{\phi^2}{\omega^2\tilde{\rho}_{22}}\bar{\nabla}\hat{p} \cdot \bar{\hat{\nabla}}\bar{\hat{q}}\, \mathrm{d}\Omega_{\mathrm{p}} + \int_{\Omega_{\mathrm{p}}} \frac{\phi^2}{\tilde{R}}\hat{p}\,\bar{\hat{q}}\, \mathrm{d}\Omega_{\mathrm{p}} + \int_{\Omega_{\mathrm{p}}} \left(\tilde{\gamma} + \tilde{\xi}\right)\hat{\mathbf{u}} \cdot \bar{\hat{\nabla}}\bar{\hat{q}}\, \mathrm{d}\Omega_{\mathrm{p}} + \int_{\Omega_{\mathrm{p}}} \tilde{\xi}\,\bar{\nabla} \cdot \hat{\mathbf{u}}\,\bar{\hat{q}}\, \mathrm{d}\Omega_{\mathrm{p}} = 0,\end{aligned} \tag{A.3}$$

where $\bullet$ denotes the scalar product of second order tensors, $\tilde{\xi} = \phi(1 + \tilde{Q}/\tilde{R})$, and $\bar{\hat{\mathbf{w}}} = \bar{\mathbf{w}}\exp(-\mathrm{i}\tilde{\mathbf{k}} \cdot \mathbf{x})$ is the periodic test function for $\hat{\mathbf{u}}$. Moreover, the stress tensor depends only on the periodic displacement field of solid phase, namely,

$$\hat{\boldsymbol{\sigma}} = \hat{A}\left(\bar{\nabla} \cdot \hat{\mathbf{u}}\right)\mathbf{I} + \tilde{N}\left(\bar{\nabla}\hat{\mathbf{u}} + \bar{\nabla}^{\mathrm{T}}\hat{\mathbf{u}}\right). \tag{A.4}$$

Similarly, the weak formulation for the periodic field representation of the elastic domain Ω_{e} can be written as:

$$\mathcal{WF}_{\mathrm{e}} = \int_{\Omega_{\mathrm{e}}} \omega^2\rho_{\mathrm{e}}\,\hat{\mathbf{u}} \cdot \bar{\hat{\mathbf{w}}}\, \mathrm{d}\Omega_{\mathrm{e}} - \int_{\Omega_{\mathrm{e}}} \hat{\boldsymbol{\sigma}}_{\mathrm{e}}(\hat{\mathbf{u}}) \bullet \bar{\hat{\nabla}}\bar{\hat{\mathbf{w}}}\, \mathrm{d}\Omega_{\mathrm{e}} = 0, \tag{A.5}$$

where ρ_{e} is the mass density od elastic material, while the periodic field of elastic stress tensor $\hat{\boldsymbol{\sigma}}_{\mathrm{e}}$ depends on $\hat{\mathbf{u}}$ and the Lamé coefficients λ_{e} and μ_{e} of the isotropic material of inclusions as follows

$$\hat{\boldsymbol{\sigma}}_{\mathrm{e}} = \lambda_{\mathrm{e}}\left(\bar{\nabla} \cdot \hat{\mathbf{u}}\right)\mathbf{I} + \mu_{\mathrm{e}}\left(\bar{\nabla}\hat{\mathbf{u}} + \bar{\nabla}^{\mathrm{T}}\hat{\mathbf{u}}\right). \tag{A.6}$$

It should be noted that we have skipped surface integrals in the weak formulation of poro-elasticty (A.3) and elasticity (A.5), because they are irrelevant for the configuration analysed in this work. Moreover, in this formulation the coupling on the interface between the poro-elastic and elastic media is natural, and since the elastic inclusion is embedded in the poro-elastic domain and has no direct contact with air the only non-zero coupling integral appears on the interface between the acoustic and poro-elastic domains:

$$\mathcal{IC}_{\text{p-a}} = \int_{\Gamma_{\text{p-a}}} \hat{\mathbf{u}} \cdot \mathbf{n}\, \bar{\tilde{q}}\, \mathrm{d}\Gamma_{\text{p-a}} + \int_{\Gamma_{\text{p-a}}} \hat{p}\, \mathbf{n} \cdot \bar{\tilde{\mathbf{w}}}\, \mathrm{d}\Gamma_{\text{p-a}}, \tag{A.7}$$

Thus, the weak formulation for the whole coupled system is: $\mathcal{WF}_{\text{a}} + \mathcal{WF}_{\text{p}} + \mathcal{WF}_{\text{e}} + \mathcal{IC}_{\text{p-a}} = 0$.

References

[1] L. M. Brekhovskikh, Waves in Layered Media, Second Edition, Elsevier, 1980.

[2] J.-P. Groby, A. Wirgin, L. De Ryck, W. Lauriks, R. P. Gilbert, Y. S. Xu, Acoustic response of a rigid-frame porous medium plate with a periodic set of inclusions, J. Acoust. Soc. Am. 126 (2) (2009) 685–693. doi:10.1121/1.3158936.
URL `https://doi.org/10.1121/1.3158936`

[3] J.-P. Groby, O. Dazel, A. Duclos, L. Boeckx, L. Kelders, Enhancing the absorption coefficient of a backed rigid frame porous layer by embedding circular periodic inclusions, J. Acoust. Soc. Am. 130 (6) (2011) 3771–3780. doi:10.1121/1.3652865.
URL `http://asa.scitation.org/doi/10.1121/1.3652865`

[4] C. Lagarrigue, J. P. Groby, V. Tournat, O. Dazel, O. Umnova, Absorption of sound by porous layers with embedded periodic arrays of resonant inclusions, J. Acoust. Soc. Am. 134 (6) (2013) 4670–4680. doi:10.1121/1.4824843.
URL `http://asa.scitation.org/doi/10.1121/1.4824843`

[5] A. Krynkin, O. Umnova, A. Y. B. Chong, S. Taherzadeh, K. Attenborough, Scattering by coupled resonating elements in air, J. Phys. D 44 (12) (2011) 125501.

[6] J.-P. Groby, C. Lagarrigue, B. Brouard, O. Dazel, V. Tournat, B. Nennig, Enhancing the absorption properties of acoustic porous plates by periodically embedding Helmholtz resonators, J. Acoust. Soc. Am. 137 (2015) 273. doi:10.1121/1.4904534.
URL `https://doi.org/10.1121/1.4904534`

[7] T. Weisser, J.-P. Groby, O. Dazel, F. Gaultier, E. Deckers, S. Futatsugi, L. Monteiro, Acoustic behavior of a rigidly backed poroelastic layer with periodic resonant inclusions by a multiple scattering approach, J. Acoust. Soc. Am. 139 (2) (2016) 617–629. doi:10.1121/1.4940669.
URL `http://asa.scitation.org/doi/10.1121/1.4940669`

[8] T. G. Zieliński, Modelling of poroelastic layers with mass implants improving acoustic absorption, in: Proceedings of ICA2007 – 19th International Congress on Acoustics, 2-7 September 2007, Madrid, Spain, 2007.

[9] M. R. F. Kidner, C. R. Fuller, B. Gardner, Increase in transmission loss of single panels by addition of mass inclusions to a poro-elastic layer: Experimental investigation, J. Sound Vib. 294 (3) (2006) 466–472. doi:10.1016/J.JSV.2005.11.022.
URL `https://www.sciencedirect.com/science/article/pii/S0022460X05007765`

[10] T. G. Zieliński, Numerical investigation of active porous composites with enhanced acoustic absorption, J. Sound Vib. 330 (22) (2011) 5292–5308.

[11] T. G. Zieliński, M.-A. Galland, E. Deckers, Influencing the wave-attenuating coupling of solid and fluid phases in poroelastic layers using piezoelectric inclusions and locally added masses, in: W. Desmet, B. Pluymers, D. Moens, W. Rottiers

(Eds.), Proceedings of ISMA2018 International Conference on Noise and Vibration Engineering and USD2018 International Conference on Uncertainty in Structural Dynamics, 2018, pp. 1091–1103.

[12] M. A. Lewińska, J. A. van Dommelen, V. G. Kouznetsova, M. G. Geers, Towards acoustic metafoams: The enhanced performance of a poroelastic material with local resonators, J. Mech. Phys. Solids 124 (2019) 189–205. doi:10.1016/j.jmps.2018.10.006.
URL `www.elsevier.com/locate/jmps`

[13] M. A. Lewińska, J. A. van Dommelen, V. G. Kouznetsova, M. G. Geers, Broadening the attenuation range of acoustic metafoams through graded microstructures, J. Sound Vib. 483 (2020) 115472. doi:10.1016/j.jsv.2020.115472.
URL `https://doi.org/10.1016/j.jsv.2020.115472`

[14] B. Nennig, Y. Renou, J.-P. Groby, Y. Aurégan, A mode matching approach for modeling two dimensional porous grating with infinitely rigid or soft inclusions, The Journal of the Acoustical Society of America 131 (5) (2012) 3841–3852.

[15] C. Lagarrigue, J. P. Groby, O. Dazel, V. Tournat, Design of metaporous supercells by genetic algorithm for absorption optimization on a wide frequency band, Appl. Acoust. 102 (2016) 49–54. doi:10.1016/j.apacoust.2015.09.011.
URL `http://dx.doi.org/10.1016/j.apacoust.2015.09.011`

[16] L. Feng, Enhancement of low frequency sound absorption by placing thin plates on surface or between layers of porous materials, The Journal of the Acoustical Society of America 146 (2) (2019) EL141–EL144.

[17] C. Boutin, Acoustics of porous media with inner resonators, J. Acoust. Soc. Am. 134 (6) (2013) 4717–4729.

[18] C. Boutin, F.-X. Bécot, Theory and experiments on poro-acoustics with inner resonators, Wave Motion 54 (2015) 76–99.

[19] X.-F. Zhu, S.-K. Lau, Z. Lu, W. Jeon, Broadband low-frequency sound absorption by periodic metamaterial resonators embedded in a porous layer, J. Sound Vib. 461 (2019) 114922.

[20] M. A. Biot, Theory of elastic waves in a fluid-saturated porous solid. I. Low frequency range, J. Acoust. Soc. Am. 28 (1956) 168–178.

[21] M. A. Biot, Theory of propagation of elastic waves in a fluid-saturated porous solid. II. Higher frequency range, J. Acoust. Soc. Am. 28 (2) (1956) 179–191.

[22] J. Allard, N. Atalla, Propagation of sound in porous media: modelling sound absorbing materials. Second Edition, John Wiley & Sons, 2009.

[23] N. Atalla, R. Panneton, P. Debergue, A mixed displacement-pressure formulation for poroelastic materials, J. Acoust. Soc. Am. 104 (1998) 1444. doi:10.1121/1.424355.
URL `https://doi.org/10.1121/1.424355`

[24] N. Atalla, M. A. Hamdi, R. Panneton, Enhanced weak integral formulation for the mixed (u,p) poroelastic equations, J. Acoust. Soc. Am. 109 (6) (2002) 3065–3068. doi:10.1121/1.1365423.
URL `https://doi.org/10.1121/1.1365423`

[25] M. A. Biot, The elastic coefficients of the theory of consolidation, J. Appl. Mech. 15 (1957) 594–601.

[26] E. Deckers, S. Jonckheere, D. Vandepitte, W. Desmet, Modelling techniques for vibro-acoustic dynamics of poroelastic materials, Arch. Computat. Methods. Eng. 22 (2) (2015) 183–236.

[27] O. Dazel, F. Sgard, F.-X. Becot, N. Atalla, Expressions of dissipated powers and stored energies in poroelastic media modeled by {u, U} and {u, P} formulations, The Journal of the Acoustical Society of America 123 (4) (2008) 2054–2063.

[28] D. L. Johnson, J. Koplik, R. Dashen, Theory of dynamic permeability and tortuosity in fluid-saturated porous media, J. Fluid

Mech. 176 (1987) 379–402.
[29] Y. Champoux, J.-F. Allard, Dynamic tortuosity and bulk modulus in air-saturated porous media, J. Appl. Phys. 70 (4) (1991) 1975–1979.
[30] P. Debergue, R. Panneton, N. Atalla, Boundary conditions for the weak formulation of the mixed (u, p) poroelasticity problem, J. Acoust. Soc. Am. 106 (5) (1999) 2383–2390.
[31] J.-P. Groby, C. Lagarrigue, B. Brouard, O. Dazel, V. Tournat, B. Nennig, Using simple shape three-dimensional rigid inclusions to enhance porous layer absorption, J. Acoust. Soc. Am. 136 (3) (2014) 1139–1148.
[32] M. Collet, M. Ouisse, M. Ruzzene, M. N. Ichchou, Floquet-Bloch decomposition for the computation of dispersion of two-dimensional periodic, damped mechanical systems, Int. J. Solids Struct. 48 (20) (2011) 2837–2848. doi:10.1016/j.ijsolstr.2011.06.002.
[33] S. Jonckheere, Wave based and hybrid methodologies for vibro-acoustic simulation with complex damping treatments, Ph.D. thesis, KU Leuven (2015).
[34] P. S. Kurzeja, H. Steeb, About the transition frequency in biot's theory, The Journal of the Acoustical Society of America 131 (6) (2012) EL454–EL460.
[35] K. Idrisi, M. E. Johnson, D. Theurich, J. P. Carneal, A study on the characteristic behavior of mass inclusions added to a poro-elastic layer, J. Sound Vib. 329 (20) (2010) 4136–4148. doi:10.1016/j.jsv.2010.04.001.
[36] C. Audet, J. E. Dennis, Pattern search algorithms for mixed variable programming, SIAM J. Optim. 11 (3) (2000) 573–594. doi:10.1137/S1052623499352024.
URL `https://scholarship.rice.edu/handle/1911/101991`
[37] C. Audet, J. E. Dennis, Analysis of generalized pattern searches, SIAM J. Optim. 13 (3) (2003) 889–903. doi:10.1137/S1052623400378742.
URL `http://www.caam.rice.edu/`

List of Tables

List of Figures